International Journal of Heat and Mass Transfer 255 (2026) 127877

Contents lists available at ScienceDirect

International Journal of Heat and Mass Transfer

journal homepage: www.elsevier.com/locate/hmt

Molecular dynamics simulation study on thermophysical properties of carbon nanotube-enhanced lithium fluoride as a high-temperature phase change material

Amir Mohammad Rahimzadeh Abdi [a], Shidvash Vakilipour [a], Jafar Al-Zaili [b,*]

[a] College of Interdisciplinary Science and Technology, University of Tehran, Tehran, Iran
[b] Department of Engineering, City St George's, University of London, Northampton Square, London, UK

ARTICLE INFO

Keywords:
Molecular dynamics
Phase change materials
Latent heat thermal energy storage
Concentrated solar power

ABSTRACT

Lithium fluoride is combined with single-walled carbon nanotubes to enhance its performance as a phase change material for using the latent heat thermal energy storage approach in concentrated solar power systems. Molecular dynamics simulation using Large-scale Atomic/Molecular Massively Parallel Simulator is employed to evaluate thermophysical properties, including density, melting point, enthalpy, specific heat capacity, thermal conductivity, diffusion coefficients, and viscosity, across both solid and liquid phases. The addition of single-walled carbon nanotube increases the density by 3.11–6.35% in the system containing 704 carbon atoms and 5.47–10.26% in the system containing 1024 carbon atoms, while enhancing the thermal conductivity by 2.76–29.42% and 17.06–33.53% in the respective systems, thereby improving volumetric energy storage and heat transfer. A reduction in melting temperature and a minor enhancement in specific heat capacity, up to 2.6% at higher carbon concentration, are also observed. Diffusion coefficients are reduced by up to 33% and viscosity by up to 35% at higher SWCNT concentrations, demonstrating the material's suitability for stationary thermal energy storage systems. Figure of merit analysis indicates that the composite phase change material with 1024 carbon atoms exhibits the best overall performance. These findings highlight the potential of single-walled carbon nanotube-enhanced lithium fluoride as a composite phase change material for thermal energy storage applications, validating the effectiveness of molecular dynamics simulations for high-temperature composite phase change material optimization in concentrated solar power systems.

1. Introduction

In recent decades, solar energy has emerged as a leading renewable resource due to its environmental advantages, including being free, renewable, and non-polluting [1]. Among various technologies for harvesting solar energy, the concentrating solar power (CSP) plants have received considerable attention for their ability to produce reliable, safe, and efficient clean energy for large-scale power generation [2,3]. However, the intermittent nature of solar energy, particularly during nighttime or cloudy conditions, poses challenges in balancing energy supply and demand. To address this limitation, CSP systems are typically integrated with thermal energy storage (TES) technologies, enabling the dispatchable and cost-effective generation of electricity from solar energy.

In CSP systems, latent heat thermal energy storage (LHTES) is of interest due to its high energy storage density, slight volume change, and ability to maintain a nearly constant operating temperature [4]. Among the LHTES approaches, solid–liquid phase change is particularly popular due to its reduced volume and phase change, high energy density, limited subcooling, and enhanced safety, especially in engineering applications [5]. At the core of these systems is phase change material (PCM), whose thermophysical properties directly affect the storage efficiency [6]. Accordingly, recent research has focused on addressing the key limitations of PCMs by improving thermal conductivity and stability, reducing supercooling, corrosion, and cost, and also enhancing overall storage performance [7–9]. These strategies include the development of advanced PCM compositions, nanoparticle incorporation [10], and encapsulation techniques [11]. Yan et al. [12] demonstrated that expanded graphite (EG) encapsulation of nitrates significantly enhances thermal conductivity (2.2 W/m K), thermal response and stability across phase transitions.

To improve the efficiency of next-generation CSP systems, their operating temperatures have been significantly increased through the im-

* Corresponding author.
E-mail address: jafar.alzaili@citystgeorges.ac.uk (J. Al-Zaili).

https://doi.org/10.1016/j.ijheatmasstransfer.2025.127877
Received 10 May 2025; Received in revised form 31 August 2025; Accepted 21 September 2025
Available online 29 September 2025

plementation of supercritical carbon dioxide (sCO_2) power cycles [13]. This increase in temperature, combined with the limitations of conventional commercial salts as PCMs, complicates the integration of TES systems and highlights the need for more advanced materials. High temperature performance also poses additional experimental and operational challenges. Key parameters for selecting and designing suitable PCMs for CSP include melting temperature, thermal stability, vapor pressure, heat capacity, density, thermal conductivity, and viscosity, all of which affect system performance and design [14–17]. Among these, thermal conductivity has been identified as the most important factor for LHTES performance. For instance, Hoshi et al. [17] conducted theoretical and numerical analyses to compare the thermal charging and discharging performance of nitrates, chlorides, carbonates, and fluorides in large-scale CSP systems. They highlighted the thermal conductivity as the most critical factor for LHTES. Smirnov et al. [18] measured the thermal conductivity of molten alkali halides (fluorides, chlorides, bromides, iodides) and their mixtures as a function of temperature. It was observed that heat transfer in ionic melts occurred as a discrete process due to the presence of ions and long-range Coulomb interactions, rather than being continuous throughout the entire volume.

Molecular dynamics (MD) simulations are a valuable tool in the development of advanced PCMs with complex compounds, especially when experimental measurements under high-temperature CSP conditions are too difficult or impractical [19–21]. It could predict vital properties with minimum simulation error. To address such issues and overcome the defects in the material properties used as PCMs, basic salts were often compounded with additives to achieve the desired properties. This provided an alternative solution to changing component concentration or mixing salts. The superior composite phase change material (CPCM) for TES in CSP applications was introduced by Yu et al. [21] with the aid of MD simulations. A 38.59% increase in thermal conductivity and a 5.87% increase in specific heat capacity were achieved by adding single-walled carbon nanotubes (SWCNT) to NaCl. However, this additive resulted in a decrease in melting point and enthalpy. The effects of several nanoparticles, such as CuO, Al_2O_3, and SiO_2, on the thermal storage performance of NaCl at high operating temperatures in the particular application were also studied using MD [22–25]. The study showed that the addition of CuO increased shear viscosity, thermal conductivity, and specific heat capacity by up to 8.12%, 9.51%, and 2.07%, respectively, but decreased melting enthalpy by 18.77% [23]. The addition of Al_2O_3 improved thermal conductivity by 15.45% [24] and 17.94% [25], as well as specific heat capacity by 7.63% [24], although it reduced the melting point and melting enthalpy [25]. SiO_2 was found to enhance thermal conductivity and shear viscosity by up to 44.2% and 23.6%, respectively [22]. MD simulation of SiO_2, coupled with $KNaCl_2$, was conducted by Zhou et al. [25], revealing that this additive increased thermal conductivity and specific heat by up to 25.28% and 7.87%, respectively. Luo et al. [26] evaluated the LHTES properties of $LiNO_3$/NaCl with six different ceramic nanoparticles (NPs). It was found that MgO nanoparticles improved thermal conductivity and specific heat capacity in the solid phase by 63.5% and 32.3%, respectively, while the total energy storage density increased to 671.7 J/g. All of these studies reported that adding the nanoparticle improved PCM's TES properties, such as thermal conductivity, specific heat capacity, etc.

Although many studies have explored different salts and composites as potential PCMs, the elevated operating temperatures and demanding conditions of next-generation CSP systems require materials with greater consistency and higher thermal conductivity to ensure efficient heat storage and transfer. Since the main aim of the present work is to identify superior PCM for LHTES in CSP, the latent heat of fusion (ΔH), melting Temperature (T_m), and thermal conductivity (λ) are assumed to be major parameters for selection of base salt(s). These properties of some salts available in the literature are depicted in Fig. 1. Lithium fluoride (LiF) is found to have a higher latent heat of fusion and thermal conductivity. While it is not considered a perfect salt in all aspects, it is superior in the critical properties. Therefore, it is chosen as a favorable candidate for the base salt of the composite.

In CSP and LHTES applications, thermal conductivity is a critical performance parameter. This property can govern the rate and efficiency of heat transfer in CSP systems. Higher thermal conductivity ensures rapid heat transfer during charging (liquefying) and discharging (solidification) cycles, which reduces unfavorable thermal gradients and improves system response times. It minimizes hotspots and ensures that the PCM melts or solidifies uniformly, improving reliability and thermal efficiency. Improved heat transfer reduces the amount of material and the size of the TES systems required, lowering costs and space requirements. For CSP systems, the PCM's thermal conductivity must be sufficiently high to enable efficient heat transfer during both the charging/discharging processes. Optimizing this property is essential for achieving high thermal efficiency in TES systems.

However, many pure salts used as PCM or heat transfer fluids inherently show low thermal conductivity. To overcome this defect, carbon-based materials—especially those with high thermal conductivity and absorption properties—have been investigated as performance enhancers [30]. Increased thermal conductivity leads to faster heat storage and release and improved overall system performance [31]. Shaikh et al. [32] showed that the addition of only 1% SWCNT resulted in a 13% increase in PCM thermal conductivity. Yu et al. [21] increased the overall thermal transport and storage performance of NaCl as PCM by incorporating SWCNT. SWCNT could also increase the thermal conductivity and specific heat capacity of another PCM based on KNO_3 up to 28.01% and 16.55%, respectively [33]. Tao et al. [34] researched the addition of various types of nanocarbon materials into carbonate eutectic salts to improve the performance of high-temperature salt PCMs. They introduced SWCNT as the optimal enhancer due to its 56.98% enhancement in the thermal conductivity of the selected PCM. SWCNT is chosen for the present study because it consists of a single layer of graphene, formed cylindrically, which results in fewer defects, more uniformity, and an extensive specific surface area [30]. Yan et al. [35] used EG as a skeleton material to enhance the thermal conductivity of polyethylene glycol (PEG), achieving values up to 2.48 W/m K while maintaining high latent heat and improving photo/electro-thermal conversion efficiency.

In the present study, LiF is screened as the base salt of a PCM due to its favorable thermophysical properties and significant potential for high-temperature thermal energy storage. Then, it is combined with SWCNT to enhance its thermal performance and make it more compatible to extend the applicability of this novel composite PCM in next-generation CSP systems operating at elevated temperatures. Classical MD simulation is employed to model this composite and calculate the temperature-dependent thermophysical properties of the LiF-SWCNT nanocomposite across a wide temperature range in both solid and liquid phases. This approach addresses a critical applicable engineering challenge in CSP technology by offering a fundamental understanding of the material's performance, enabling the optimization of its composition and structure for improved key parameters of heat storage/transfer efficiency, such as density, thermal conductivity, and specific heat capacity of PCM operating under extreme thermal conditions in advanced solar thermal energy storage applications. In addition, these findings contribute essential data for the rational design and optimization of TES in CSP applications by providing the required thermophysical properties of CPCM with good accuracy at the special conditions of these power plants.

2. Model and simulation method

The present MD simulations are carried out using Large-scale Atomic/Molecular Massively Parallel Simulator (LAMMPS) software [36]. In the first step, the Materials Project database is used for simulating pure LiF [37]. Unit cell data for LiF (mp-1138) were retrieved from

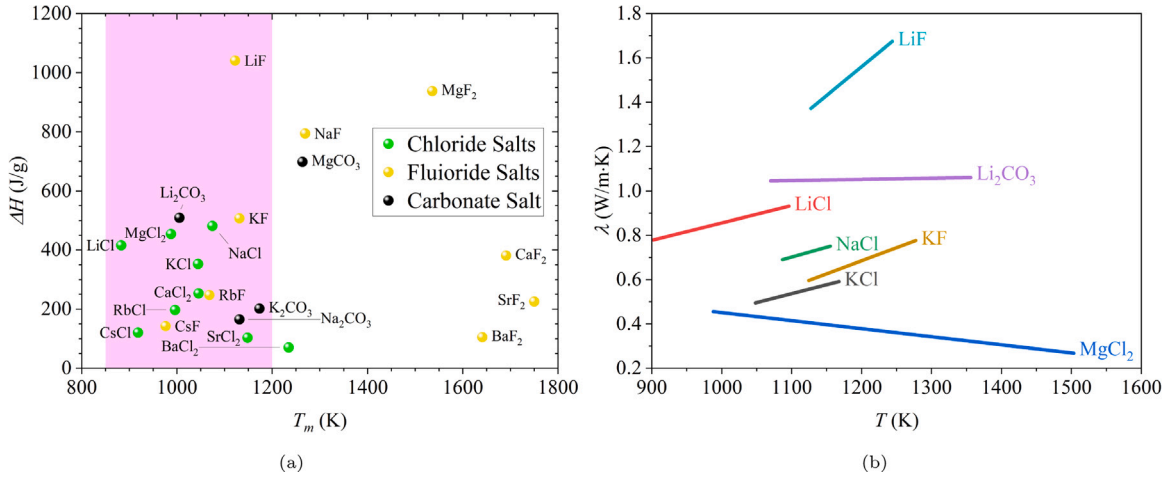

Fig. 1. Main criteria for salt selection. (a) Enthalpy (latent heat) of fusion as a function of melting temperature [27], (b) temperature variation of thermal conductivity [18,28,29] for selected salts.

the Materials Project database version v2023.11.1. The LiF (mp-1138) is experimentally measured in numerous literature references within this database. Comprehensive information about the crystal structure of this selected unit cell is available on the relevant website [38]. In brief, the Lattice constant is 4.08 Å and $\alpha = \beta = \gamma = 90°$. This unit cell is extended $10 \times 10 \times 10$ in three dimensions of X, Y, and Z using AtomSK software [39], as shown in Fig. 2(a). Finally, the size of the initial configuration is X: 0–40.8 Å, Y: 0–40.8 Å, Z: 0–40.8 Å, containing 4000 Li^+ and 4000 F^-. The charges of anions and cations are set to $+e$ and $-e$, respectively.

Similarly, the structure of SWCNT is produced as an additive using the nanotube builder extension of Visual Molecular Dynamics (VMD) software [40]. Both nanotube chiral indices, n and m, are chosen as 16 to produce an armchair CNT. The length of the CNT is determined so that the number of carbon atoms is 704 and 1024, respectively. The produced neutral CNT is inserted into the LiF crystal lattice using AtomSK to create composite phase change materials (CPCM), as shown in Fig. 2(b). The mass fraction of SWCNT in the CPCM was calculated from the ratio of the total SWCNT mass to the combined mass of SWCNT and LiF atoms. Accordingly, the systems containing 0, 704, and 1024 carbon atoms in the SWCNT correspond to 0 wt%, 7.53 wt%, and 10.60 wt% SWCNT, respectively.

In this study, the interaction between LiF atoms is described using the Buckingham potential. This potential, which is closely related to the Born–Mayer–Huggins (BMH) potential, can be converted to each other [42]. These potentials have been proven to be a good choice for calculating the thermophysical properties of fluoride salts such as LiF, especially during phase changes [43]. The concept behind these potentials is the rigid ion model (RIM). In this model, electronic polarization is assumed to be neglected, and each ion is considered to carry a unit-point fixed charge at its center of mass [44]. The function of this force field with Coulomb interaction is defined in the LAMMPS code as follows [45]:

$$U_{ij}^{BUCK} = \frac{q_i q_j}{r_{ij}} + A_{ij}^{BUCK} \exp\left(\frac{-r_{ij}}{\rho}\right) - \left(\frac{C_{ij}^{BUCK}}{r_{ij}^6}\right) \tag{1}$$

where q_i and q_j are formal charges, and r_{ij} represents the distance between the centers of two ions. A_{ij}^{BUCK} C_{ij}^{BUCK} are repulsion parameters and the Van der Waals parameter in the Buckingham potential, respectively. ρ is the hardness parameter. The Buckingham terms (the second and third ones) are only calculated in short ranges ($r < r_c$, where r_c is the cutoff radius). The short-range cut-off radius (r_c) in Buckingham terms is assumed to be 12 Å for calculations related to LiF salt. However, Coulomb's term is used to calculate the long-distance electrostatic interaction by solving the particle–particle particle-mesh (PPPM) method [46] with an accuracy of 10^{-5}. The PPPM solver, utilizing Fourier transforms, had a scale of $N \log N$ (N is the number of atoms). This typically resulted in significantly faster performance for large periodic systems compared to alternative methods [47] such as the Ewald method (where cost scales as $N^{(3/2)}$), etc. The Buckingham potential parameters for LiF are shown in Table 1, which are taken from MD work by Gruenhut and MacFarlane [48]. Adaptive Intermolecular Reactive Empirical Bond Order AIREBO potential [49], which is commonly used and accurate for carbon systems [50], is employed to describe the interactions of the C atoms in SWCNT. The function of this potential in LAMMPS is described in the relevant manual [45]. A cutoff distance of 10.2 Å is used for r_c between C atoms.

Table 1
Buckingham potential parameters for LiF [48].

Pair	A_{ij}^{BUCK} [eV]	ρ [Å]	C_{ij}^{BUCK} [eV Å^6]
Li–Li	120.20	0.2857	0.1600
Li–F	309.00	0.2840	1.7900
F–F	495.00	0.3039	22.300

Finally, the Lennard-Jones potential (L-J potential) [51] is used to determine the atomistic interaction between LiF atoms and carbon atoms. Its function in LAMMPS is as follows:

$$U_{ij}^{LJ} = 4\epsilon_{ij}\left(\left(\frac{\sigma_{ij}}{r_{ij}}\right)^{12} - \left(\frac{\sigma_{ij}}{r_{ij}}\right)^{6}\right) \tag{2}$$

where r is the distance between two atoms. ϵ is the depth of the potential well, which represents how strongly the atoms attract each other. σ is the finite distance at which the inter-particle potential is zero, representing the distance where repulsive and attractive forces balance. A cutoff distance, r_c of 12 Å, is also set for this potential.

To determine the potential parameters, the Lorentz–Berthelot mixing rules are followed:

$$\epsilon_{ij} = \sqrt{\epsilon_{ii} \times \epsilon_{jj}} \tag{3}$$

$$\sigma_{ij} = \frac{\sigma_{ii} + \sigma_{jj}}{2} \tag{4}$$

These derived parameters, following this rule, are also matched with the data from work by Kumar and Seminario [52].

The hybrid potential command in LAMMPS enables the utilization of these three potential functions and relevant parameters for CPCM in one simulation. To maintain a constant number of atoms in the simulation system, remove boundary effects, and achieve bulk behavior, a periodic boundary condition is applied along all three dimensions (X,

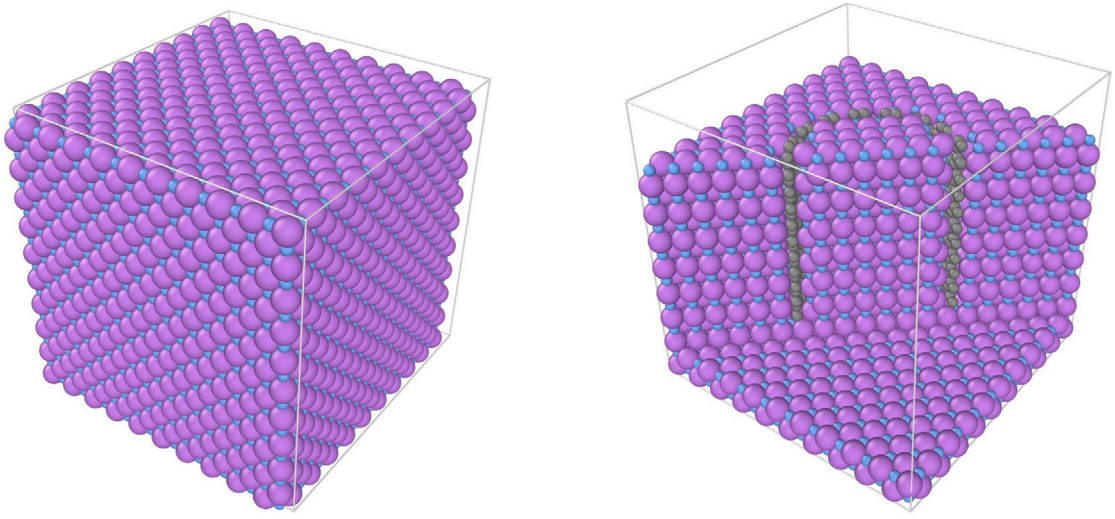

Fig. 2. Initial configuration of simulation systems visualized by OVITO software [41]. (a) Pure LiF supercell and (b) the slice of a composite system includes inserted carbon atoms. Purple, light blue, and gray spheres represent Lithium (Li^+), Fluoride (F^-) ions, and Carbon (C) atoms, respectively. (For interpretation of the references to color in this figure legend, the reader is referred to the web version of this article.)

Y, and Z), in all cases. Time steps of 1 femtosecond (fs) are used for the whole of the simulations. The Verlet algorithm is utilized to solve Newton's equations of motion.

Before the start of the main simulation sequences, all systems underwent energy minimization via the standard conjugate gradient algorithm. The systems are gradually heated up to 300 K under the NVT ensemble in 2.5 ns, then a pressure of 1 bar is applied by the NPT ensemble for 2.5 ns. This sequence is repeated to ensure an equilibrated state is reached in the first stage. The total simulation time for this equilibrium stage is 10 nanoseconds (ns). The systems are then heated up to the next target temperature by the NVT ensemble in 1 ns, and at each temperature, the NPT ensemble applies a pressure of 1 bar for 1 ns to reach the equilibrium state again. The NVE ensemble is used for the calculations of thermophysical properties for 1 ns. The Nose–Hoover [53] thermostat and barostat are utilized to regulate the system's temperature and pressure, respectively. Exactly similar sequences are followed for the cooling process. The temperature steps and ranges for both heating and cooling processes are selected at 100 K, and the temperature range is 300–2000 K, respectively. The initial equilibrating, heating, and cooling processes took 80 ns of simulation time. All simulations were run on the Hyperion high-performance computing cluster at City St George's, University of London. Parallel processing was implemented using the OpenMPI distributed memory model, with each system running on six nodes. Each node was equipped with two Intel Xeon Gold 6248R processors and 384 GB of RAM.

2.1. Evaluated properties

The density is a crucial thermophysical property of molten salt-based PCM because it is related to volumetric heat capacity and the usable capacity of PCMs in the CSP system. As such, it had a direct effect on the economy of CSP. The density of the simulation system on an atomic scale is calculated as follows:

$$\rho = \frac{N M}{N_A V} \tag{5}$$

where ρ is the density of the simulated system (g/cm^3), N is the number of atoms present in the system, M is the molar mass (g/mol), V is volume of system in the equilibrated state at the target temperature and pressure (cm^3) and N_A is Avogadro's constant (mol^{-1}). In such simulations, the correct density is achieved by following an NPT ensemble.

The transition temperature from solid to liquid of CPCM is shown by T_m. This is a critical temperature that directly determines the operating temperature of the system. T_m (K) is calculated directly by recording and monitoring the enthalpy of the system. It is the temperature at which phase transition evidence is observed during the heating process of the simulation system to a much higher expected melting temperature.

One of the most conspicuous pieces of evidence of phase change is observed by recording the total enthalpy with temperature change, especially during the heating process. Usually, the total enthalpy of the system increased linearly with the system temperature, but this increment grew sharply near the melting point. For this purpose, the enthalpy jump during the heating process is considered more reliable because the supercooling phenomenon is more probable during the cooling process [8].

The specific heat capacity c_p, at constant pressure, is governed by the enthalpy value. To calculate the heat absorbed or released during temperature variations and overall energy density, this parameter plays a key role in TES systems. It is calculated during the heating process from solid-state to liquid-state in the NPT ensemble, and it is obtained by:

$$c_p = \left(\frac{\partial H}{\partial T}\right)_P = \frac{1}{k_B T^2}\langle \delta(E_K + U + PV)^2 \rangle \approx \frac{\Delta H}{\Delta T \rho V} \tag{6}$$

where H is the total enthalpy of the system (kJ/mol), k_b, E_k, U, P, V and T are the Boltzmann constant, kinetic energy (kJ/mol), potential energy (kJ/mol), pressure (Pa), volume (m^3) and temperature (K) of the system respectively. the melting enthalpy ΔH is defined as the change in total enthalpy during the phase transition, expressed in (J/g).

Based on Einstein's law of diffusion, the self-diffusion coefficients D of various CPCM systems are calculated as follows:

$$D = \frac{1}{2N}\lim_{t\to\infty}\frac{\partial}{\partial t}\langle |r_i(t) - r_i(0)|^2 \rangle \tag{7}$$

In this function, D is the coefficient of self-diffusion (m^2/s) for CPCM. N here is the dimension of the simulation system, and t is the calculation time (s) of the simulation. r_i is the second position of the atom type i in the simulation system after passing simulation time of t. The angle bracket here represents ensemble averaging. The thermodynamic state of the atoms during simulations, which followed the TES performance of the CSP, is proportional to this parameter, especially in the liquid state [21]. Time-dependent mean square displacement (MSD)

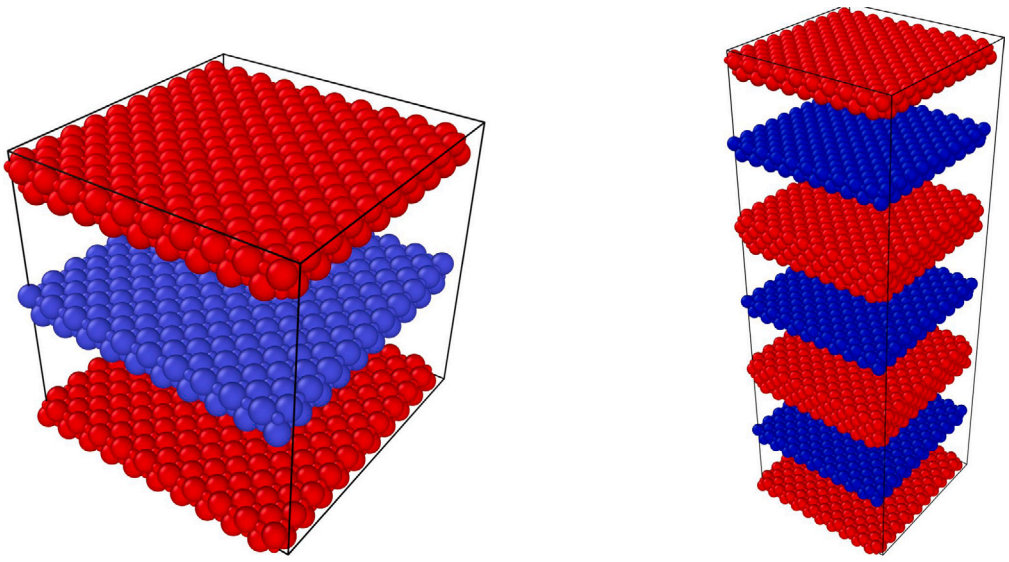

Fig. 3. Non-equilibrium molecular dynamics (NEMD) simulations. The top and bottom bins are the hottest (red color) region, and the middle one is the coldest (red color) region (a). The periodic boundary condition is shown in the Z direction (b). (For interpretation of the references to color in this figure legend, the reader is referred to the web version of this article.)

can be used to calculate the above angle bracket, which represents ion transmission. The MSD results used for diffusion coefficient evaluation, and also a more detailed explanation of the atomistic parameters used in this study, including the radial distribution function (RDF) and coordination number (N), are provided in Appendix.

Thermal conductivity is the most important thermal property of PCM in CSP because it determines the capability of heat transfer of the system. In addition, this property is the major defect of PCMs, so it is the main aim of this research. Fourier's law of heat conduction, as shown below, is the concept behind the calculation of this property via nonequilibrium molecular dynamics (NEMD):

$$\lambda = -\frac{Q}{A \cdot \nabla T} \tag{8}$$

where λ is the thermal conductivity of the CPCM (W m^{-1} K^{-1}), Q is the nonequilibrium steady heat flow in the unit of time, A is the cross-sectional area of the simulation system (m^2). ∇T is the gradient of temperature across the system (K m^{-1}). In NEMD, the target simulation system is uniformly divided into equal segments in one direction. In this work, CPCM systems are divided into 20 segments, called bins, in the Z direction. Then, the temperatures of the first and last bins are controlled by a Langevin thermostat at +50 K higher than the simulation target temperature. Other hot segments are created automatically beside those in the neighboring boxes due to the periodic boundary conditions in all directions (Fig. 3(b)). In addition, the temperature of the middle bin is also controlled by an identical thermostat but at −50 K lower than the simulation target temperature (Fig. 3(a)). This technique produced a nonequilibrium steady heat flow of Q between the hot and cold segments.

The NEMD simulation sequences started after the systems followed the explained simulation sequences in the previous sections at each target temperature. At this point, the CPCMs are relaxed under another NVT ensemble for 1 ns to ensure equilibration at the target temperature. Next, the system is equilibrated for 1 ns under the NVE ensemble, but the described Langevin thermostats are applied during this time. Finally, after the system is equilibrated and the desired linear temperature gradient is stabilized, the thermal conductivity is calculated by:

$$\lambda = -\frac{Q}{L_x L_y \langle \frac{\partial T}{\partial Z} \rangle} \tag{9}$$

where L_x, L_y represented the lengths of the system along the X and Y axes (Å), respectively. The imposed temperature gradient ∇T is determined by calculating $\partial T/\partial z$, which indicates the rate of temperature change per unit length in the Z direction.

The ability of the matter to resist deformation under shear stress is measured as shear viscosity. It determines the transport needs, such as the pump hydraulic head in CSPs. In the present study, the time integration of a stress autocorrelation function (SACF) based on the Green-Kubo formula [54], in conjunction with equilibrium molecular dynamics (EMD) simulations, is applied to calculate the viscosity of CPCM systems.

$$\eta = \frac{1}{k_B T V} \int_0^{+\infty} \langle P_{xy}(0)\, P_{xy}(t) \rangle \tag{10}$$

where η is the shear viscosity, k_B is the Boltzmann constant, T and V are the temperature and volume of the CPCM system. P_{xy} is the pressure tensor component at time t in the XY directions. The angle bracket represents the average value of the autocorrelation function.

2.2. Performance comparison

Accurate optimization of the PCM in high-temperature CSP applications requires comprehensive knowledge of system details, including scale, geometry, operating conditions, regional factors, engineering constraints, etc. While these factors vary from one design to another, the common performance goals in such multi-objective optimization include maximizing storage capacity, heat transfer, and hydrodynamic performance. To enable a meaningful and quantitative comparison among the simulated CPCM systems, the Figure of Merit (FoM) approach was used to evaluate their overall performance. The FoM provides a quantity to characterize the performance of a system based on key functional properties. The derived thermophysical properties of the CPCM, such as thermal conductivity, specific heat capacity, melting enthalpy, density, and viscosity, significantly influence the performance of LHTES systems in CSP applications. Three general FoMs, tailored to such storage systems, were introduced and validated in the works of Tripathi and Marconnet [55] and Binotti et al. [56] as follows:

$$FoM_{LH} = \lambda^{0.5} \rho^{0.5} \Delta H^{0.5} \tag{11}$$

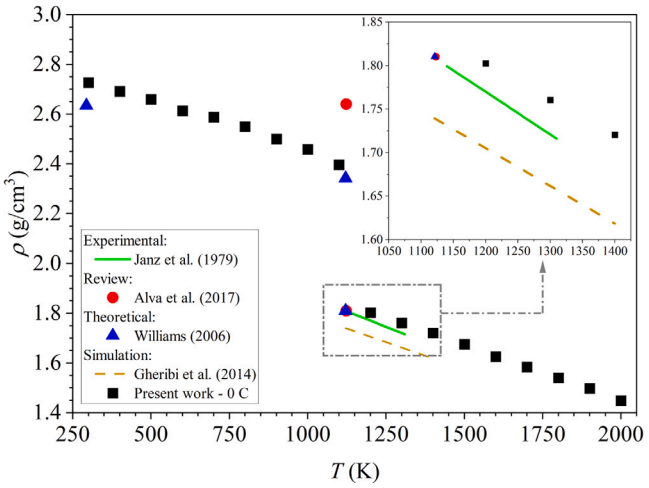

Fig. 4. Temperature variation of density for pure LiF, i.e., 0 C CPCM, in comparison with experimental [57], review [58], theoretical [59], and simulation [60] results.

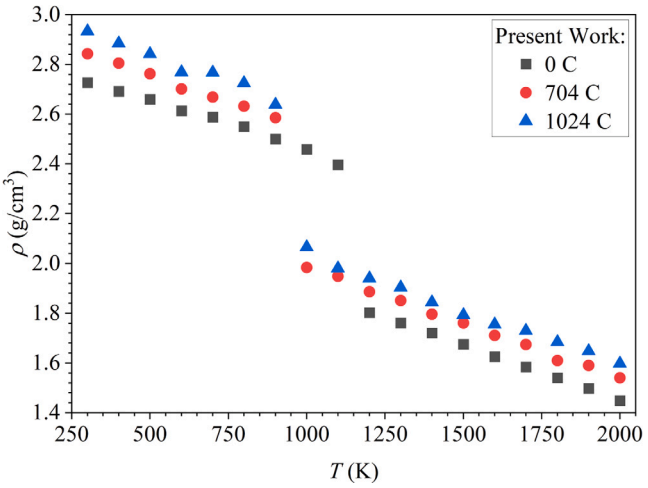

Fig. 5. Temperature variation of density for CPCM systems with 0 C, 704 C, and 1024 C.

$$FoM_{HX} = \frac{\rho^{0.3} c_p^{0.6} \lambda^{0.6}}{\eta^{0.2}} \tag{12}$$

$$FoM_{HP} = \frac{\rho^{2} c_p^{2.8}}{\eta^{0.2}} \tag{13}$$

FoM_{LH} focuses on the material's latent heat storage potential, making it a useful indicator for assessing energy storage effectiveness in LHTES systems. FoM_{HX} emphasizes the material's heat storage and transfer properties, which are crucial for the performance of heat exchangers that perform a key function in LHTES systems. FoM_{HP} reflects viscosity and density, as they influence the hydrodynamic behavior and flow efficiency in systems.

3. Results and discussions

3.1. Evaluated properties

Density plays a crucial role in heat transfer and thermal energy storage, significantly impacting the size of the TES systems. A higher-density material requires less volume to store an equivalent amount of energy. The simulated density of pure LiF is shown in Fig. 4, alongside available data from the literature. In this regard, the density of all systems decreases with increasing temperature in both solid and liquid phases. This reduction is due to the increased volume of the systems (size of the simulation box in MD). In this simulation, the density of the systems is calculated after equilibration and pressure application via the NPT ensemble at each target temperature. The maximum discrepancy between the experimental and calculated density of molten pure LiF in the present work is 2.61%, which occurs at 1400 K.

In the solid phase, the available data concerning the temperature dependence of the density of pure LiF is limited. Alva et al. [58] in a review article and Williams [59] in a theoretical study reported the density of pure LiF at restricted temperatures in the solid phase. At a temperature of 1100 K, the calculated density of LiF shows a 2.4% and 9.2% discrepancy with the values reported by Williams [59] and Alva et al. [58], respectively. Although Alva et al. [58] did not specify the exact temperature of their reported values, they just reported solid density, liquid density, and melting point. For comparison, it is assumed that these values are taken at the reported melting temperature. These minimal discrepancies in both solid and liquid phases indicate that the calculation methodology and potential energy function employed in this study are valid, ensuring that the results are reliable.

The calculated density of different systems with inserted 704 and 1024 carbon atoms, i.e., 704 C and 1024 C, is shown in Fig. 5. Similarly, the density decreases with increasing temperature due to the increased system volume. However, the density of CPCM at all temperatures increases with the addition of carbon atoms. In the solid region, the density increases by 3.11–4.19% with the addition of 704 C and by 5.47–7.55% with the addition of 1024 C, whereas in the liquid region the corresponding increases are 4.37–6.35% and 7.02–10.26%, respectively. This indicates that adding SWCNT into LiF enhances its density and improves its TES characteristics as a PCM. A higher-density mass requires less volume to store an equivalent amount of energy, making it a promising candidate for improved TES performance. In the context of CSP, this means that more thermal energy can be stored within a given volume of PCM, improving the thermal storage unit's efficiency and compactness. This is an important consideration for the cost, spatial, and material requirements of the storage in large-scale solar power plants. This improvement supports the development of more compact and efficient TES systems suitable for integration into advanced CSP technologies.

In these figures, a sharp change of density is observed around 1200 K for 0 C CPCM, which could be considered as evidence of the phase transition. This temperature point can be assumed to correspond to the melting temperature. A similar phenomenon is observed around 1000 K for the 704 C and 1024 C CPCM systems, suggesting that phase changes also occur in these composites. The observed decrease in phase transition temperature with the addition of SWCNT further supports the conclusion that incorporating carbon nanotubes into LiF facilitates a reduction in the melting temperature of the composite material.

The variations in total enthalpy with respect to temperature during the heating process are shown in Fig. 6. It is clear that the enthalpy increases as the temperature rises in all CPCM systems. Notably, the enthalpy curves exhibit a sharp rise near the melting point, which corresponds to the phase transition occurring in the systems. In 0 C CPCM (pure LiF), this sudden increase in the enthalpy occurred at 1182 K, which is only 5.44% higher than the experimental melting temperature reported by Janz et al. [57]. Higher estimation of melting temperature is commonly observed in MD simulations of ionic salts, as reported in several similar studies [21,61,62]. The superheating is attributed to the absence of free surfaces and crystal defects with periodic boundary conditions, as well as the mismatch between the number of atoms in the simulation model and the actual atoms, as explained in previous MD works [61,63]. The melting temperature and enthalpy calculated for 0 C, 704 C, and 1024 C systems are described in Table 2. According to Table 2, the insertion of SWCNT into pure LiF leads to a decrease in the

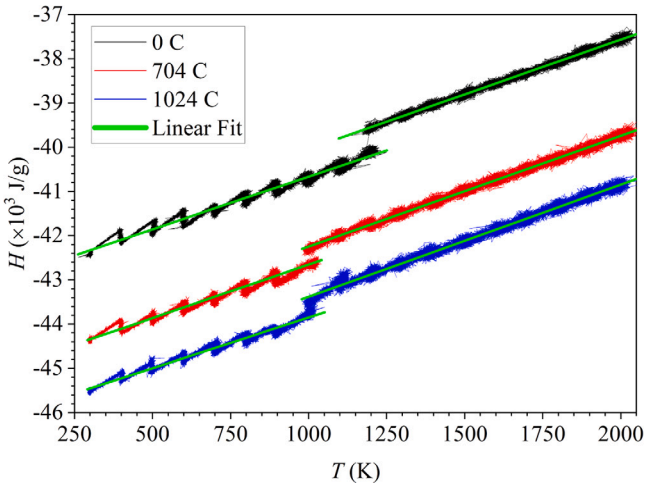

Fig. 6. Temperature variation of total enthalpy of systems. (For interpretation of the references to color in this figure legend, the reader is referred to the web version of this article.)

Table 2
Comparison of experimental values (pure LiF only) and simulated CPCM properties at various SWCNT loadings.
Source: Extracted from Fig. 6.

Parameter	Experimental	Present work		
		0 C	704 C	1024 C
Melting temperature (T_m) [K]	1121 [57]	1182	1000	996
Melting enthalpy (ΔH) [J/g]	1040 [57]	868.27	472.06	547.19
Specific heat capacity (c_p) [J/mol K]	64.2 [65,66]	61.77	62.70	63.36

melting temperature. However, increasing the number of carbon atoms has a minimal effect on the phase transition temperature in the CPCM systems. Similar behavior has been reported in prior research, which shows that nanoparticles do not always lead to a predictable trend in T_m [64]. Due to their extremely high melting temperature, SWCNT does not engage in the phase transition process and therefore have limited influence on the melting temperature of the composite. According to the extensive review by Said et al. [64], changes in melting temperature resulting from nanoparticle incorporation typically remain within a ±20% range.

The jumps in enthalpy during the phase transition can be used to evaluate the latent heat of fusion, or the melting enthalpy. This amount can be calculated by:

$$\Delta H = H_l - H_s \tag{14}$$

where H_l and H_s represent the enthalpies of the liquid and solid phases close to the melting point, respectively. The change in enthalpy ΔH is extracted from Fig. 6, then the corresponding values for different systems are shown in Table 2. The experiments performed by Janz et al. [57] measured ΔH for bulk LiF by 1040 J/g, while their calculations estimated it with 868.3 J/g. These results show a 16.5% discrepancy between the experiments and the calculation. It is important to note that classical MD simulations require careful selection of accurate potential functions and parameters; however, the precision in predicting enthalpy is often limited [67]. For instance, the enthalpy calculation error for NaCl is 18.4% [21] and for KNO_3, 30.0% [68], making the current calculation error of 16.5% acceptable for the utilized method and material. There is a difference in the characteristics of phase transitions observed in experiments compared to those predicted by MD simulations [33]. In the experimental method, materials are continuously heated, resulting in a complete solid–liquid phase transition. However, during MD simulation, some atoms penetrate inside the CNT and form a nanolayer around it. Moreover, the temperature increases too rapidly, preventing the complete solid–liquid phase transition. These factors contribute to the discrepancy between the experimental results and the molecular dynamics (MD) predictions. The value of ΔH initially decreases by 45.6% with the addition of 704 carbon atoms. However, when the number of carbon atoms in the system is increased to 1024 C, the value of ΔH is restored and even increases, as shown in Fig. 6 and summarized in Table 2. Reducing ΔH by adding carbon is an unavoidable negative side effect of using nano-enhancers [69].

In general, when both PCM and SWCNT absorb heat to reach the phase transition temperature of CPCM, the salt undergoes a phase change process, whereas SWCNT does not, thus limiting their overall latent heat. Shaikh et al. [32] The intermolecular attraction can be divided into two classes of short-range and long-range forces. In context of phase change materials, the chemical potential energy is associated with weak van der Waals attractions, while strong ionic and covalent bonds (long-range forces) play a significant role in determining the latent energy of the PCM material [32]. In nano-enhanced PCM, the close interaction between nanoparticle and the PCM can influence long-range molecular forces, especially at higher nanoparticle concentrations. If the interaction between the nanoparticle and the PCM becomes greater than the interaction among PCM molecules themselves, the heat of fusion may increase. A larger surface area, utilizing smaller nano-enhancers such as SWCNT, and greater dispersion ability are reported to improve intermolecular attraction with the PCM and nanoparticle, hence increasing latent heat. The findings of the current study are consistent with this result, where increasing the number of carbon atoms from 704 to 1024 led to a greater surface area. This increase in surface area enhanced the interaction between the nanoparticle and the PCM, resulting in a higher melting enthalpy. This suggests that at 1024 carbon atoms, the increased surface area and stronger interactions play a dominant role. In contrast, at 704 atoms, the reduction in melting enthalpy is more influenced by the non-melting enthalpy of the additive. Many contributing factors, such as size, concentration, surface area, shape, and even the intermolecular attraction between the nanoparticle and PCM, can affect the latent heat behavior of CPCM. Furthermore, it is evident from the literature that the effect of nanoparticle addition on the latent heat of PCM does not follow a general trend [64,70] owing to the conflicting effects of the contributing factors.

In Fig. 6, the solid green line represents a linear fit for the enthalpy of the systems. According to Eq. (6), the slope of this fitted curve is employed to calculate the specific heat capacity (c_p) of all systems. The extracted value of c_p for various systems is presented succinctly in Table 2. The difference between the calculated and experimental values [65, 66] of this property for LiF is 3.8%. Reported specific heat (c_p) values in this way represent an average over the simulated temperature interval, consistent with the experimental data cited, which are also presented as single averaged values rather than temperature-dependent functions. As the number of carbon atoms is increased in the system, no significant change in c_p is observed. Only a 2.6% increase is noted as the number of carbon atoms increased from 0 to 1024. Specific heat capacity is a vital parameter governing the amount of heat a material can store over a given temperature interval. Thus, even modest improvements can contribute to increased energy storage density and thermal efficiency in high-temperature TES systems. The observed increase in specific heat capacity (c_p) is mainly due to the larger effective surface area formed at the interface between the nanoparticle and the PCM [26]. This expanded interfacial region facilitates improved thermal interaction, enhancing the overall heat storage capability of the composite. Therefore, incorporating SWCNT into the designed CPCM improves the TES characteristics of the base salt (LiF) as a PCM.

In this study, the nonequilibrium molecular dynamics (NEMD) method is employed to calculate the thermal conductivity of the CPCM system, which has a finite length L_z in the Z-direction. Fig. 7 illustrates the thermal conductivity of pure LiF over a wide range

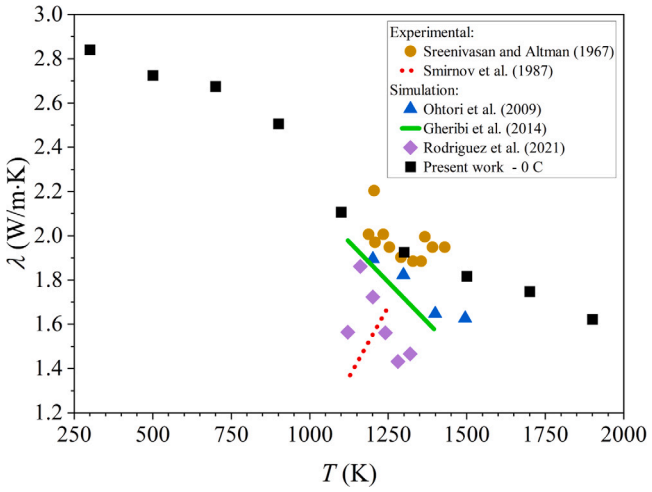

Fig. 7. Temperature variation of thermal conductivity for pure LiF, i.e., 0 C CPCM, in comparison with experimental [18,71] and simulation [65,72,73] results.

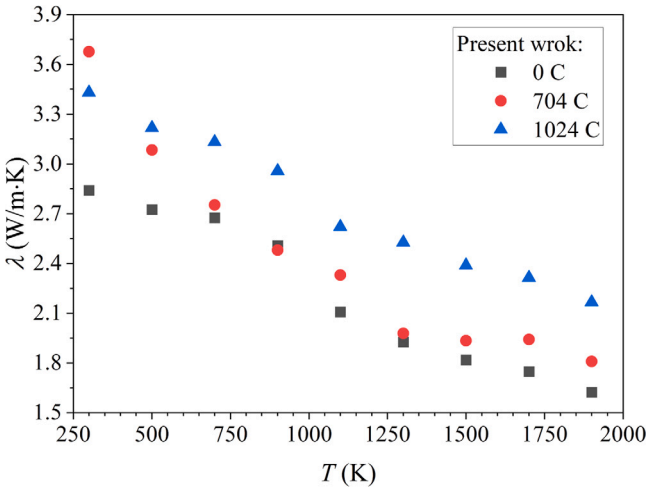

Fig. 8. Temperature variation of thermal conductivity of CPCM systems for three different concentrations of SWCNT: 0 C, 704 C, and 1024 C.

of temperatures, compared with experimental data [18,71] and prior simulation studies [65,72,73]. The thermal conductivity values obtained in the present study are found to be in excellent agreement with experimental and simulated references, particularly in the temperature range of 1000–1400 K (the lower temperature of the molten phase). This validation confirmed the accuracy of the interatomic potentials and computational methods employed, reinforcing the reliability of MD simulations in predicting thermal conductivity for high-temperature applications.

Fig. 8 highlights the thermal conductivity of CPCM systems for three different concentrations of single-walled carbon nanotubes (SWCNT): 0 C, 704 C, and 1024 C. It is observed that thermal conductivity decreased as the temperature increased. However, an increase in the concentration of SWCNT from 0 C to 1024 C resulted in an enhancement of the thermal conductivity. Across the studied temperature range, the addition of 704 C enhances the thermal conductivity by 2.76–29.42%, while the incorporation of 1024 C results in a greater improvement of 17.06–33.53% compared with pure LiF. It is concluded that the addition of nanoparticles, such as SWCNT, can significantly improve thermal conductivity by forming heat-conductive networks within the CPCM system. At the atomic scale, the primary cause of thermal conductivity enhancement is the development of a network structure formed between the SWCNT and PCM. Likewise, SWCNT tends to relocate toward the grain boundary of PCM and develop continuous quasi-2D bundles [74]. These regions act as interconnected thermal bridges, providing efficient pathways for phonon transport across the CPCM. As a result, they reduce thermal resistance and promote directional heat flow, leading to improved thermal conductivity. From the composite aspect (macroscopic level), the SWCNT possesses extremely high inherent thermal conductivity and thus plays a reinforcing role across the CPCM matrix.

Finally, this enhancement is found to improve the thermal performance and efficiency of high-temperature TES applications, particularly those working in conjunction with the sCO_2 cycle. Enhanced thermal conductivity not only supports faster heat exchange but also contributes to the overall efficiency and responsiveness of the TES unit. These results underscore the potential of carbon nanotube-reinforced PCMs in meeting the demanding heat transfer requirements of next-generation CSP.

The self-diffusion coefficient of Li and F in the liquid phase is illustrated in Figs. 9(a) and 9(b), respectively. The available experimental data [75] on this property are limited; however, the calculated values of D for both Li and F are found to be in good agreement with the experimental results. Moreover, the simulated values of D in the pure LiF system are in good agreement with two valuable MD simulation results [73,76]. Furthermore, it is observed that the calculated diffusion coefficients are lower than the experimental values, which may be attributed to the calculated melting temperature of LiF being higher than the experimentally determined value, in contrast to what is observed by Luo et al. [76].

The diffusion coefficient of both Li and F is suppressed by an increment in the number of carbon atoms of SWCNT in the system. This property is observed to increase with rising temperatures in all systems. The diffusion coefficient of F decreases by 18.27–23.19% and 27.39–33.51% for the 704 C and 1024 C systems, respectively. In parallel, the diffusion coefficient of Li decreases by 16.26–21.66% and 23.19–28.60% for the respective systems In the solid phase, a lower diffusion coefficient minimizes heat loss through thermal conduction, improving thermal insulation during storage periods. This helps to retain stored heat for longer durations, thereby improving the system's efficiency. After melting, a higher diffusion coefficient facilitates better heat transfer within the liquid PCM by enhancing convective and conductive heat flow. It supports faster and more uniform temperature distribution, reducing the time required for charging (melting) and discharging (solidifying) cycles. Typically, the addition of nanoparticles (e.g., SWCNT) is found to enhance the effective thermal conductivity of the PCM, indirectly affecting the diffusion of heat without significantly altering its fundamental diffusion coefficient.

Viscosity is closely related to the diffusion coefficient, with empirical evidence indicating that higher diffusion coefficients are typically associated with lower viscosities [76]. This property is only defined in the liquid phase, and consequently, Eq. (10) is only valid for this particular phase in the MD simulation. Fig. 10 depicts the variation of viscosity with temperature for pure LiF. At a temperature of 1300 K, a maximum error of 10.8% is observed with the result reported by Janz et al. [57]. At this temperature and other higher temperatures, however, the estimated η is found to be very close to the experimental result reported by Abe et al. [77] for pure LiF. It is observed that increasing temperature is followed by a decrease in viscosity in all systems. Moreover, viscosity is found to decrease more rapidly at lower temperatures compared to higher temperatures, and its variation with increasing temperature follows a pattern similar to an exponential function. The viscosity trends support the suitability of LiF and CPCM systems for TES applications, as lower viscosity at higher temperatures facilitates better thermal transport and flow properties in CSP systems. As shown in Fig. 11, adding more SWCNT is found to lead to an increase in the viscosity of CPCMs. The viscosity decreases by 3.93–15.27% and

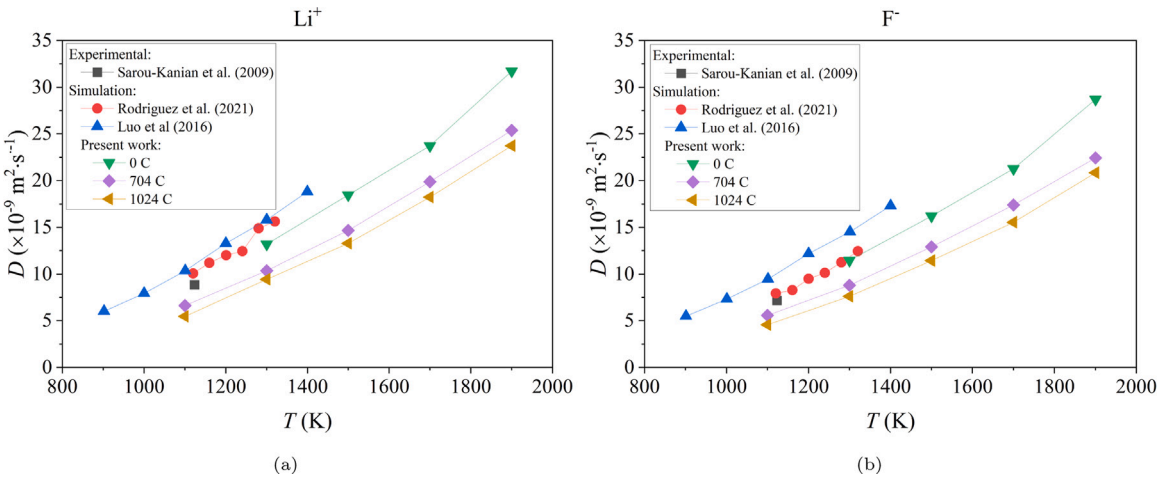

Fig. 9. Temperature variation of diffusion coefficients of systems for (a) Li^+ ion, (b) F^- ion. The presented experimental values are reported by Sarou-Kanian et al. [75], and simulation values are reported by Luo et al. [76] and Rodriguez et al. [73].

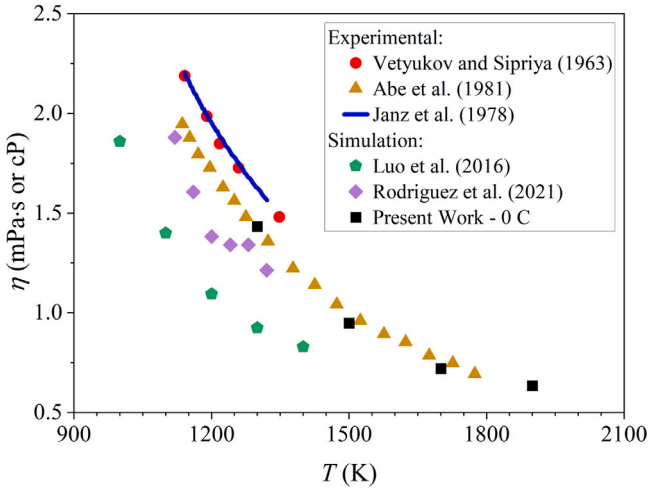

Fig. 10. Temperature variation of viscosity for pure LiF, i.e., 0 C CPCM, in comparison with experimental [77,79] and simulation [73,76] results.

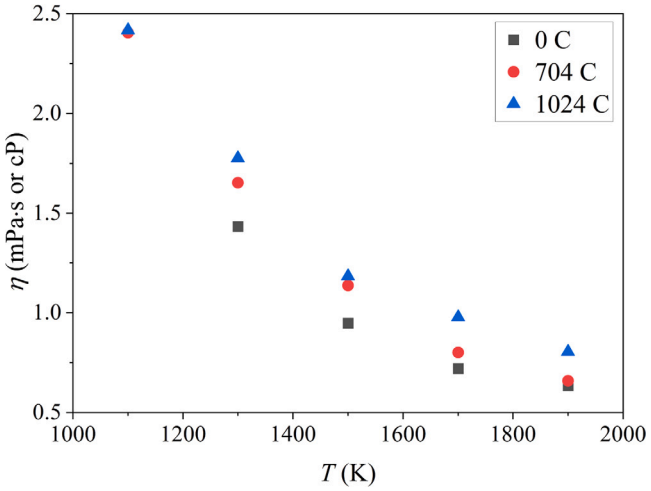

Fig. 11. Temperature variation of viscosity for CPCM systems with 0 C, 704 C, and 1024 C.

23.84–35.44% for the 704 C and 1024 C systems, respectively, indicating a more significant reduction at higher carbon content. Notably, the trends are consistent with those observed in pure LiF, suggesting that the addition of components in CPCMs does not significantly disrupt the general thermophysical trends. A similar result was observed in the MD investigation of Liu and Xiao [78] when they added a nanoparticle to enhance the properties of solar salt as a TES medium in CSP. They found that, due to the enhanced interaction between ions in the base fluid, the viscosity of the TES materials increases with an increase in the mass fraction of nanoparticles.

Generally, increasing viscosity due to pumping and transport requirements is not favorable for a storage material in TES applications [69]. However, in this study, it is assumed that the simulated CPCM acts as an almost stationary PCM in the relevant storage tanks and/or heat exchangers in CSPs. Therefore, in this particular type of application, the enhancement of thermal storage behavior, which is related to thermal conductivity, specific heat capacity, etc., is given more priority than the transport behavior, which is related to viscosity. Nevertheless, Jiang et al. [80] provided a comprehensive discussion on balancing energy density and pumping power and also defined criteria for this purpose, depending on the design of the TES system in CSP, which can be used for further design and engineering purposes.

3.2. Performance comparison

The calculated values of FoM for the simulated CPCM systems at a temperature of 1300 K are presented in Table 3. A temperature near the phase change is selected, and the calculated FoM values are scaled to the range of 0 to 1 to facilitate comparison. The CPCM includes 1024 C exhibiting the highest values of FoM_{HX} and FoM_{HP}, indicating excellent suitability in aspects of heat exchanger and hydrodynamic performance. However, due to a decrease in melting enthalpy in the carbon-containing systems, which directly impacts FoM_{LH}, this system ranks second in that criterion. Based on this overall evaluation, the 1024 C CPCM is recommended as the most suitable system, as it achieves the highest performance in both thermal transfer and hydrodynamic aspects, while exhibiting only a marginal reduction in the latent heat criterion.

It is obvious that the reduction in melting enthalpy is not desirable, and it can limit the latent heat storage capacity. However, this limitation can be compensated in practice by design strategies such as adjusting the storage volume, etc. In contrast, insufficient thermal conductivity poses a more fundamental constraint. For this reason, improving thermal conductivity is considered a more important priority

Table 3
Values of FoM for the simulated CPCM systems at temperature of 1300 K.

FoM	0 C	704 C	1024 C
FoM_{LH}	0.294	0.173	0.263
FoM_{HX}	0.088	0.089	0.103
FoM_{HP}	0.145	0.155	0.162

in the development and practical use of CPCMs from both engineering and application perspectives.

4. Conclusions

The development of high-performance TES systems for CSP applications is hindered by the limitations of conventional PCMs, particularly their low thermal conductivity and limited stability at elevated operating temperatures. In this study, classical MD simulations were employed to comprehensively evaluate the thermophysical behavior of a novel LiF-SWCNT composite PCM under CSP-relevant extreme conditions. Three systems with different carbon concentrations were considered: 0C (pure LiF), 704C, and 1024C.

The results revealed that:

- Density (ρ): In the solid region, the density increased by 3.11–4.19% with the addition of 704 carbon atoms and by 5.47–7.55% with the addition of 1024 carbon atoms. In the liquid region, the corresponding increases were 4.37–6.35% and 7.02–10.26%, respectively. This increment enhances volumetric energy storage capacity, which is particularly beneficial for CSP applications where maximizing stored energy per unit volume improves system compactness and efficiency.
- Thermal conductivity (λ): Across the studied temperature range, the addition of 704 carbon atoms enhanced thermal conductivity by 2.76–29.42%, while the incorporation of 1024 carbon atoms produced a larger improvement of 17.06–33.53% compared with pure LiF. Higher thermal conductivity accelerates heat transfer during charging and discharging, reduces thermal gradients, and improves the overall efficiency of TES systems in CSP applications.
- Specific heat capacity (c_p): The incorporation of SWCNT produced a modest enhancement in c_p, with increases of up to 2.6% at higher carbon concentrations. Even this slight improvement contributes to greater energy storage per unit mass, supporting improved TES performance in CSP applications.
- Melting temperature (T_m) and enthalpy (ΔH): SWCNT presence reduced the melting temperature and decreased the melting enthalpy compared with pure LiF. The observed reduction in melting temperature, when properly managed, may help broaden the operational temperature range, while the concurrent enhancement in thermal conductivity offsets the reduction in melting enthalpy by improving overall heat transfer efficiency in TES systems.
- Diffusion coefficient (D) and viscosity (η): In the liquid phase, embedding SWCNTs reduced the diffusion coefficients of Li^+ and F^- ions by up to 33%, while viscosity decreased by up to 35% compared with the 0 C system. Both properties remain within acceptable ranges for stationary TES applications.

Experimental investigation of LiF–SWCNT at the elevated temperatures required for CSP, particularly those employing advanced sCO_2 power cycles, remains technically challenging, and available data across solid and liquid phases are scarce. This highlights the importance of MD simulations as a predictive tool for evaluating novel composite PCMs. Our results show improvements in density, thermal conductivity, and specific heat capacity, alongside reductions in melting temperature, enthalpy, diffusion coefficients, and viscosity, which may require attention in future optimization studies.

In summary, LiF-SWCNT shows synergistic improvements in key thermophysical properties, making it a strong candidate for next-generation TES materials in high-temperature CSP plants with sCO_2 cycles. FoM analysis identified the 1024-carbon system as achieving the highest overall performance. These findings highlight the promise of LiF-SWCNT and confirm the value of MD simulations as a reliable tool for designing and optimizing composite PCMs under extreme operating conditions.

CRediT authorship contribution statement

Amir Mohammad Rahimzadeh Abdi: Writing – original draft, Visualization, Software, Methodology, Formal analysis. **Shidvash Vakilipour:** Writing – original draft, Supervision, Investigation. **Jafar Al-Zaili:** Writing – original draft, Supervision, Software, Conceptualization.

Declaration of competing interest

The authors declare that they have no known competing financial interests or personal relationships that could have appeared to influence the work reported in this paper.

Appendix. Atomic-scale structural/dynamic analysis

This appendix provides supplementary information regarding the atomistic-level parameters used to characterize the structural and transport behavior of the LiF-SWCNT systems, namely the radial distribution function (RDF), mean square displacement (MSD), and coordination number (N), as derived from molecular dynamics simulations.

Overall MSD is utilized to measure the dynamics of a system. It can be used to study how the dynamics of a system change with temperature and the number of particles in the system. The mean squared displacement is a measure of how much the atoms in a system move around over time. Fig. A.12 shows MSD as a function of time for Li-F systems at different temperatures. The plots also show how the mean squared displacement changes with temperature. As the temperature increases, the mean squared displacement increases. This is because the atoms in the system have more thermal energy, which causes them to move around more. As a result, the average distance that an atom moves over time increases. Also, it is seen that the MSDs are too small and almost constant in solid temperatures (see inset graphs in Fig. A.12). These confirm low movement of atoms in the correct simulation in solid-state. In addition, a transition in time evolution of MSD is predicted at the temperature of 1100 K for 0 C CPCM (Fig. A.12(a)) and 900 K for 704 C and 1024 C CPCMs, see Figs. A.12(b) and A.12(c). These changes in the behavior of atoms can be caused by phase transitions, which have been confirmed in other results, such as enthalpy. Also, as explained in the previous section, MSD can be used to compare the diffusion capabilities of atoms in CPCMs with varying mass fractions of SWCNT in the liquid state. According to the comparison graphs in Fig. A.12, the magnitude of MSD is decreased as the number of carbon atoms of SWCNT is increased in the systems. Therefore, the addition of SWCNT can lead to a restricted transferability of atoms in the system.

RDF is used to provide structural information about the PCM system. It is defined as [21]:

$$g_{mn}(r) = \frac{dN_{mn}(r)}{4\pi\rho_n r^2 dr} \tag{A.1}$$

where $g_{mn}(r)$ represents the RDF of CPCM, $N_{mn}(r)$ is the number of the atom species n distributed in the sphere shell of radius r (Å), which is centered by the atom species m. ρ_n is the number density of the atom species n in the entire simulation system, expressed in ($Å^{-3}$).

Direct observation of CPCM's structural changes is challenging during phase transformations in experiments. To overcome this, the radial distribution function (RDF) is calculated for various CPCM systems

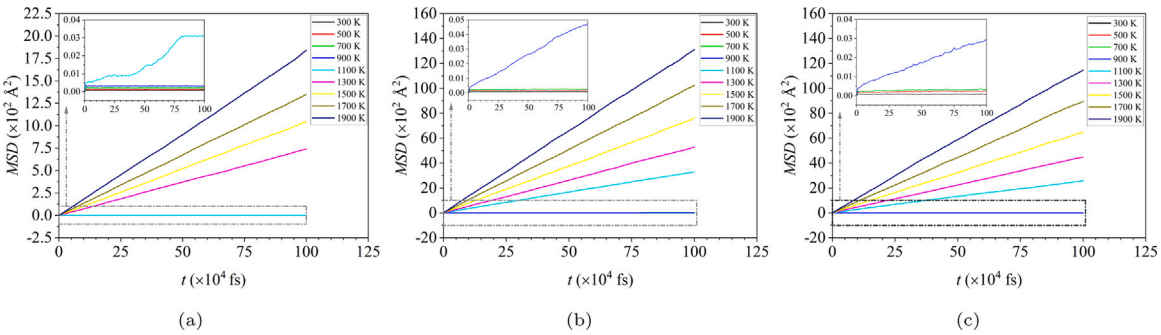

Fig. A.12. Temperature variation of MSD of systems for (a) 0 C, (b) 704 C, and (c) 1024 C CPCM.

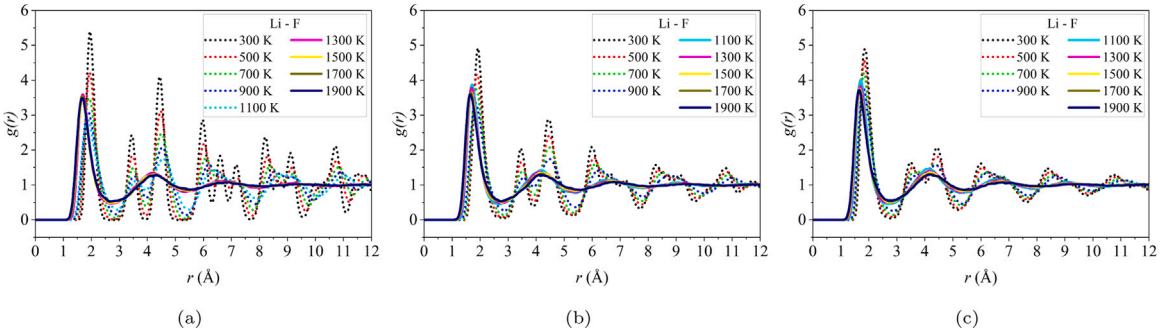

Fig. A.13. Temperature variation of RDF of systems for (a) 0 C, (b) 704 C, and (c) 1024 C CPCM. Dotted and solid lines denote solid and liquid temperatures, respectively.

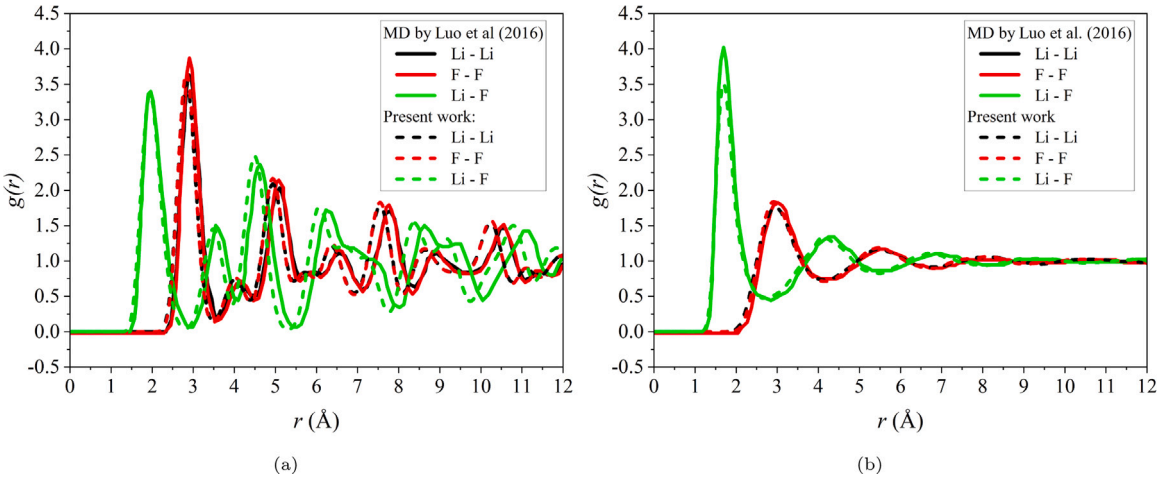

Fig. A.14. RDF of pure LiF (0 C CPCM) at temperatures of (a) 600 K and (b) 1400 K in comparison to MD simulation reported by Luo et al. [76] (solid lines).

at different temperatures. Fig. A.13 demonstrates RDFs and provides insights into the microstructural evolution of CPCM during phase transitions. Fig. A.14 shows the radial distribution function for pure LiF, detailing the atomic correlations between Li-Li, F-F, and Li-F. The results are compared with the MD data from Luo et al. [76]. The similarity in the peak positions and intensities validates the present work. The minor discrepancies between the two data sets could stem from differences in the computational methodologies or potential types and parameters used.

In both Figs. A.14(a) and A.13 The RDFs of CPCM systems exhibit several distinct peaks at various distances when the temperature is below the melting point. This pattern reflects microstructures characterized by both short-range and long-range order, indicating that the CPCMs are in a solid state. Moreover, as the temperature increases, the heights of the RDF peaks decrease, while their widths expand. When the temperatures of CPCMs rise above the melting point (around 1100 K for 0 C CPCM and approximately 900 K for 704 C CPCM and 1024 C CPCM), the RDFs exhibit a prominent first peak that rapidly diminishes with increasing distance. This indicates that the microstructures of the CPCMs transition to short-range order and long-range disorder, signifying a liquid state. Thus, it can be concluded that the melting temperature of 0 C CPCM is around 1100–1300 K, and for 704 C CPCM and 1024 C CPCMs are in the temperature range of 900–1100 K, which are agreed with the observed enthalpy results in the previous sections. As the temperature increases, the system transitions from a solid to a liquid state, with the phase transformation evident from the changes in the RDFs.

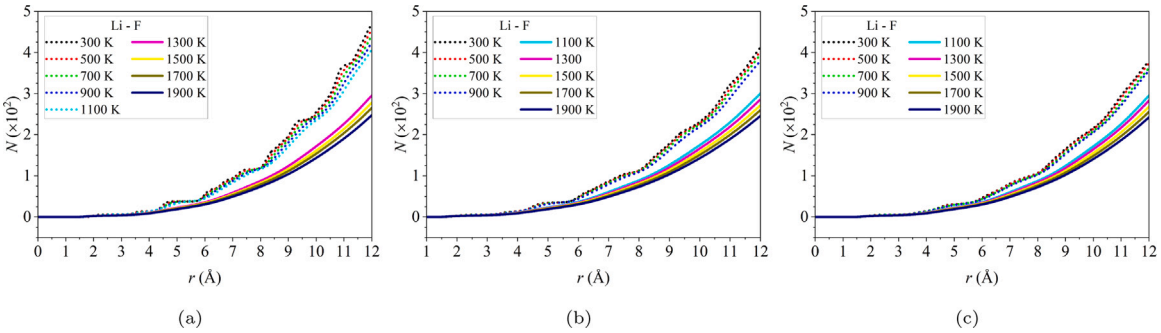

Fig. A.15. Temperature variation of N of systems for (a) 0 C, (b) 704 C, and (c) 1024 C CPCM. The dotted line is set for solid temperatures, and the solid line for liquid ones.

The coordination number (N_{mn}) is another crucial parameter that provides insights into the local structural characteristics of the system [42]:

$$N_{mn} = 4\pi \int_0^{r_{min}} g_{mn}(r) \cdot r^2 dr \tag{A.2}$$

N_{mn} is the average number of i-type ions in a sphere with j-type ions as the center and a radius of r_{min}, which is the position of the first valley of the RDF.

Fig. A.15 presents the coordination number (N) for Li–F interactions at various temperatures, evaluated for three systems: A.15(a) 0C CPCM, A.15(b) 704 C CPCM, and A.15(c) 1024 C CPCM.

The coordination number is the number of nearest neighbors that an atom has. In this case, it is the number of F atoms that are nearest neighbors to a Li atom. The plots also show how the coordination number changes with temperature. As the temperature increases, the coordination number decreases. This is because the atoms in the system have more thermal energy, which causes them to move around more and spread out. As a result, the average distance between atoms increases, and the number of nearest neighbors decreases. At lower temperatures, the coordination numbers exhibit steeper initial rises, indicating stronger local ordering and clustering of Li and F ions, but when the temperature increases, the slopes become gentler. The coordination number analysis highlights the temperature-dependent reduction in structural ordering within the LiF system, correlating with the results of the RDFs. As the system transitions to higher temperatures, the weaker ionic correlations reflect phase changes or structural softening, which are crucial for understanding the behavior of phase-change materials in high-temperature applications.

Data availability

Data will be made available on request.

References

[1] E. Kabir, P. Kumar, S. Kumar, A.A. Adelodun, K.-H. Kim, Solar energy: Potential and future prospects, Renew. Sustain. Energy Rev. 82 (2018) 894–900.
[2] M.T. Islam, N. Huda, A. Abdullah, R. Saidur, A comprehensive review of state-of-the-art concentrating solar power (CSP) technologies: Current status and research trends, Renew. Sustain. Energy Rev. 91 (2018) 987–1018.
[3] R. Merchán, M. Santos, A. Medina, A.C. Hernández, High temperature central tower plants for concentrated solar power: 2021 overview, Renew. Sustain. Energy Rev. 155 (2022) 111828.
[4] G. Sadeghi, Energy storage on demand: Thermal energy storage development, materials, design, and integration challenges, Energy Storage Mater. 46 (2022) 192–222.
[5] Q. Wang, C. Wu, X. Wang, S. Sun, D. Cui, S. Pan, H. Sheng, A review of eutectic salts as phase change energy storage materials in the context of concentrated solar power, Int. J. Heat Mass Transfer 205 (2023) 123904.
[6] M. Samykano, Role of phase change materials in thermal energy storage: Potential, recent progress and technical challenges, Sustain. Energy Technol. Assessments 52 (2022) 102234.
[7] C. Xu, H. Zhang, G. Fang, Review on thermal conductivity improvement of phase change materials with enhanced additives for thermal energy storage, J. Energy Storage 51 (2022) 104568.
[8] A. Safari, R. Saidur, F. Sulaiman, Y. Xu, J. Dong, A review on supercooling of phase change materials in thermal energy storage systems, Renew. Sustain. Energy Rev. 70 (2017) 905–919.
[9] M.I. Khan, F. Asfand, S.G. Al-Ghamdi, Progress in research and technological advancements of thermal energy storage systems for concentrated solar power, J. Energy Storage 55 (2022) 105860.
[10] S. Shoeibi, H. Kargarsharifabad, S.A.A. Mirjalily, M. Sadi, A. Arabkoohsar, A comprehensive review of nano-enhanced phase change materials on solar energy applications, J. Energy Storage 50 (2022) 104262.
[11] H. Peng, J. Wang, X. Zhang, J. Ma, T. Shen, S. Li, B. Dong, A review on synthesis, characterization and application of nanoencapsulated phase change materials for thermal energy storage systems, Appl. Therm. Eng. 185 (2021) 116326.
[12] K. Yan, L. Qiu, H. Li, N. Cao, Y. Feng, Expanded graphite encapsulation of nitrates for enhanced thermal transport: Mechanism insight and component screening, Compos. Sci. Technol. 259 (2025) 110957.
[13] J.-M. Yin, Q.-Y. Zheng, Z.-R. Peng, X.-R. Zhang, Review of supercritical CO2 power cycles integrated with CSP, Int. J. Energy Res. 44 (3) (2020) 1337–1369.
[14] W. Ding, T. Bauer, Progress in research and development of molten chloride salt technology for next generation concentrated solar power plants, Engineering 7 (3) (2021) 334–347.
[15] M. Sarvghad, S.D. Maher, D. Collard, M. Tassan, G. Will, T.A. Steinberg, Materials compatibility for the next generation of concentrated solar power plants, Energy Storage Mater. 14 (2018) 179–198.
[16] S. Wu, T. Yan, Z. Kuai, W. Pan, Thermal conductivity enhancement on phase change materials for thermal energy storage: A review, Energy Storage Mater. 25 (2020) 251–295.
[17] A. Hoshi, D.R. Mills, A. Bittar, T.S. Saitoh, Screening of high melting point phase change materials (PCM) in solar thermal concentrating technology based on CLFR, Sol. Energy 79 (3) (2005) 332–339.
[18] M. Smirnov, V. Khokhlov, E. Filatov, Thermal conductivity of molten alkali halides and their mixtures, Electrochim. Acta 32 (7) (1987) 1019–1026.
[19] J. Ding, G. Pan, L. Du, J. Lu, W. Wang, X. Wei, J. Li, Molecular dynamics simulations of the local structures and transport properties of Na2CO3 and K2CO3, Appl. Energy 227 (2018) 555–563.
[20] H. Tafrishi, S. Sadeghzadeh, R. Ahmadi, Molecular dynamics simulations of phase change materials for thermal energy storage: A review, RSC Adv. 12 (23) (2022) 14776–14807.
[21] Y. Yu, C. Zhao, Y. Tao, X. Chen, Y.-L. He, Superior thermal energy storage performance of NaCl-SWCNT composite phase change materials: A molecular dynamics approach, Appl. Energy 290 (2021) 116799.
[22] Y. Yu, Y. Tao, Y.-L. He, Molecular dynamics simulation of thermophysical properties of NaCl-SiO2 based molten salt composite phase change materials, Appl. Therm. Eng. 166 (2020) 114628.
[23] C. Guo, J. Wu, Y. Yu, H. Tian, Efficient thermal energy storage achieved by NaCl–CuO composite phase change material: A molecular dynamics study, J. Mol. Liq. 377 (2023) 121557.
[24] H. Tian, Z. Kou, Y. Yu, S. Tang, X. Wu, Coupled optimization of optical and thermal properties for NaCl-Al2O3 towards efficient thermal energy storage, J. Energy Storage 69 (2023) 107923.
[25] W. Zhou, Z. Yang, Y. Feng, L. Lin, Insights into the thermophysical properties and heat conduction enhancement of NaCl-Al2O3 composite phase change material by molecular dynamics simulation, Int. J. Heat Mass Transfer 198 (2022) 123422.
[26] Q. Luo, X. Liu, Q. Xu, Y. Tian, H. Yao, J. Wang, S. Lv, C. Dang, Y. Xuan, Ceramic nanoparticles enhancement of latent heat thermal energy storage properties for LiNO3/NaCl: Evaluation from material to system level, Appl. Energy 331 (2023) 120418.

[27] M.M. Kenisarin, High-temperature phase change materials for thermal energy storage, Renew. Sustain. Energy Rev. 14 (3) (2010) 955–970.
[28] H. Yang, R. Gallagher, P. Chartrand, A.E. Gheribi, Development of a molten salt thermal conductivity model and database for advanced energy systems, Sol. Energy 256 (2023) 158–178.
[29] J. Lu, S. Yang, G. Pan, J. Ding, S. Liu, W. Wang, Thermal and transport properties of molten chloride salts with polarization effect on microstructure, Energies 14 (3) (2021) 746.
[30] M. Li, B. Mu, Effect of different dimensional carbon materials on the properties and application of phase change materials: A review, Appl. Energy 242 (2019) 695–715.
[31] Z.A. Qureshi, H.M. Ali, S. Khushnood, Recent advances on thermal conductivity enhancement of phase change materials for energy storage system: A review, Int. J. Heat Mass Transfer 127 (2018) 838–856.
[32] S. Shaikh, K. Lafdi, K. Hallinan, Carbon nanoadditives to enhance latent energy storage of phase change materials, J. Appl. Phys. 103 (9) (2008).
[33] Y. Yu, Y. Tao, C. Zhao, X. Yu, Thermal storage performance enhancement and regulation mechanism of KNO3-SWCNT based composite phase change materials, Int. J. Heat Mass Transfer 181 (2021) 121870.
[34] Y. Tao, C. Lin, Y. He, Preparation and thermal properties characterization of carbonate salt/carbon nanomaterial composite phase change material, Energy Convers. Manage. 97 (2015) 103–110.
[35] K. Yan, Y. Feng, L. Qiu, Thermal and photo/electro-thermal conversion characteristics of high energy storage density expanded graphite/polyethylene glycol shaped composite phase change materials, Sol. Energy 272 (2024) 112477.
[36] A.P. Thompson, H.M. Aktulga, R. Berger, D.S. Bolintineanu, W.M. Brown, P.S. Crozier, P.J. In't Veld, A. Kohlmeyer, S.G. Moore, T.D. Nguyen, et al., LAMMPS-a flexible simulation tool for particle-based materials modeling at the atomic, meso, and continuum scales, Comput. Phys. Comm. 271 (2022) 108171.
[37] A. Jain, S.P. Ong, G. Hautier, W. Chen, W.D. Richards, S. Dacek, S. Cholia, D. Gunter, D. Skinner, G. Ceder, et al., Commentary: The materials project: A materials genome approach to accelerating materials innovation, APL Mater. 1 (1) (2013).
[38] The materials project database website, 2023, URL https://next-gen.materialsproject.org/.
[39] P. Hirel, Atomsk: A tool for manipulating and converting atomic data files, Comput. Phys. Comm. 197 (2015) 212–219.
[40] W. Humphrey, A. Dalke, K. Schulten, VMD: Visual molecular dynamics, J. Mol. Graph. 14 (1) (1996) 33–38.
[41] A. Stukowski, Visualization and analysis of atomistic simulation data with OVITO–the open visualization tool, Modelling Simul. Mater. Sci. Eng. 18 (1) (2009) 015012.
[42] X. Yang, C. Ji, J. Liu, Y. Ma, B. Cao, New insights into the heat capacity enhancement of nano-SiO2 doped alkali metal chloride molten salt for thermal energy storage: A molecular dynamics study, J. Energy Storage 63 (2023) 107015.
[43] S.A. Khrapak, M. Chaudhuri, G.E. Morfill, Freezing of Lennard-Jones-type fluids, J. Chem. Phys. 134 (5) (2011).
[44] H. Wang, Molecular Dynamics Simulations of Molten Salts: Force Field Evaluation and Development, University of Notre Dame, 2022.
[45] LAMMPS documet, 2023, URL https://docs.lammps.org/.
[46] R.E. Isele-Holder, W. Mitchell, A.E. Ismail, Development and application of a particle-particle particle-mesh Ewald method for dispersion interactions, J. Chem. Phys. 137 (17) (2012).
[47] E. Pollock, J. Glosli, Comments on P3m, FMM, and the Ewald method for large periodic Coulombic systems, Comput. Phys. Comm. 95 (2–3) (1996) 93–110.
[48] S. Gruenhut, D.R. MacFarlane, Molecular dynamics simulation of heavy metal fluoride glasses: Comparison of Buckingham and BHM potentials, J. Non-Cryst. Solids 184 (1995) 356–362.
[49] S.J. Stuart, A.B. Tutein, J.A. Harrison, A reactive potential for hydrocarbons with intermolecular interactions, J. Chem. Phys. 112 (14) (2000) 6472–6486.
[50] S.K. Sinha, D. Kumar, A. Patnaik, An investigation on thermal stability of single wall carbon nanotubes (SWCNTs) by molecular dynamics simulations, Mater. Today: Proc. 44 (2021) 4940–4944.
[51] A.K. Rappé, C.J. Casewit, K. Colwell, W.A. Goddard III, W.M. Skiff, UFF, a full periodic table force field for molecular mechanics and molecular dynamics simulations, J. Am. Chem. Soc. 114 (25) (1992) 10024–10035.
[52] N. Kumar, J.M. Seminario, Lithium-ion model behavior in an ethylene carbonate electrolyte using molecular dynamics, J. Phys. Chem. C 120 (30) (2016) 16322–16332.
[53] D.J. Evans, B.L. Holian, The nose–hoover thermostat, J. Chem. Phys. 83 (8) (1985) 4069–4074.
[54] W.G. Hoover, D.J. Evans, R.B. Hickman, A.J. Ladd, W.T. Ashurst, B. Moran, Lennard-Jones triple-point bulk and shear viscosities. Green-Kubo theory, Hamiltonian mechanics, and nonequilibrium molecular dynamics, Phys. Rev. A 22 (4) (1980) 1690.
[55] P.M. Tripathi, A.M. Marconnet, A new thermal management figure of merit for design of thermal energy storage with phase change materials, Int. J. Heat Mass Transfer 220 (2024) 124952.
[56] M. Binotti, M. Astolfi, S. Campanari, G. Manzolini, P. Silva, Preliminary assessment of sCO2 cycles for power generation in CSP solar tower plants, Appl. Energy 204 (2017) 1007–1017.
[57] G.J. Janz, C.B. Allen, N. Bansal, R. Murphy, R. Tomkins, Physical properties data compilations relevant to energy storage, 2. Molten salts: Data on single and multi-component salt systems, Nasa Sti/Recon Tech. Rep. N 80 (1979) 10643.
[58] G. Alva, L. Liu, X. Huang, G. Fang, Thermal energy storage materials and systems for solar energy applications, Renew. Sustain. Energy Rev. 68 (2017) 693–706.
[59] D.F. Williams, Additional physical property measurements and assessment of salt compositions proposed for the intermediate heat transfer loop, 2006, ORNL/GEN4/LTR-06-033.
[60] A.E. Gheribi, D. Corradini, L. Dewan, P. Chartrand, C. Simon, P.A. Madden, M. Salanne, Prediction of the thermophysical properties of molten salt fast reactor fuel from first-principles, Mol. Phys. 112 (9–10) (2014) 1305–1312.
[61] Y. Li, W. Tie, W. Tan, Q. Zhu, Molecular dynamics simulation of thermophysical properties of NaCl-KCl phase change materials applied to concentrating solar power, J. Energy Storage 52 (2022) 104707.
[62] Y. Lu, G. Zhang, J. Hao, J. Zhang, L. Chang, S. Yan, H. Zhang, Q. Cui, H. Tan, Molecular dynamics simulation of thermodynamic properties and local structure of Na2CO3-K2CO3 eutectic salt during phase transition, J. Energy Storage 43 (2021) 103221.
[63] Z. Jin, K. Lu, To what extent a crystal can be superheated, Nanostruct. Mater. 12 (1–4) (1999) 369–372.
[64] Z. Said, A. Pandey, A.K. Tiwari, B. Kalidasan, F. Jamil, A.K. Thakur, V. Tyagi, A. Sarı, H.M. Ali, Nano-enhanced phase change materials: Fundamentals and applications, Prog. Energy Combust. Sci. 104 (2024) 101162.
[65] A.E. Gheribi, J.A. Torres, P. Chartrand, Recommended values for the thermal conductivity of molten salts between the melting and boiling points, Sol. Energy Mater. Sol. Cells 126 (2014) 11–25.
[66] R.C. Gallagher, A. Birri, N.G. Russell, A.-T. Phan, A.E. Gheribi, Investigation of the thermal conductivity of molten LiF-NaF-KF with experiments, theory, and equilibrium molecular dynamics, J. Mol. Liq. 361 (2022) 119151.
[67] F. Yang, Q. Xu, Y. Xuan, J. Liu, C. Sun, Q. Luo, X. Liu, Design of elevated temperature phase change materials of carbonate-villiaumite eutectic mixtures: Method, validation, and application, Sol. Energy Mater. Sol. Cells 251 (2023) 112155.
[68] B. D'Aguanno, M. Karthik, A. Grace, A. Floris, Thermostatic properties of nitrate molten salts and their solar and eutectic mixtures, Sci. Rep. 8 (1) (2018) 1–15.
[69] Z.-R. Li, N. Hu, L.-W. Fan, Nanocomposite phase change materials for high-performance thermal energy storage: A critical review, Energy Storage Mater. 55 (2023) 727–753.
[70] J. Pereira, A. Moita, A. Moreira, An overview of the molten salt nanofluids as thermal energy storage media, Energies 16 (4) (2023) 1825.
[71] K. Sreenivasan, M. Altman, The determination of thermal diffusivities of thermal energy storage materials: Part II—Molten salts beyond the melting point, J. Eng. Power 91 (3) (1969) 189–197.
[72] N. Ohtori, T. Oono, K. Takase, Thermal conductivity of molten alkali halides: Temperature and density dependence, J. Chem. Phys. 130 (4) (2009).
[73] A. Rodriguez, S. Lam, M. Hu, Thermodynamic and transport properties of LiF and FLiBe molten salts with deep learning potentials, ACS Appl. Mater. & Interfaces 13 (46) (2021) 55367–55379.
[74] P. Vigneshwaran, S. Shaik, S. Suresh, M. Abbas, C.A. Saleel, E. Cuce, Solar salt with carbon nanotubes as a potential phase change material for high-temperature applications: Investigations on thermal properties and chemical stability, ACS Omega 8 (20) (2023) 17563–17572.
[75] V. Sarou-Kanian, A.-L. Rollet, M. Salanne, C. Simon, C. Bessada, P.A. Madden, Diffusion coefficients and local structure in basic molten fluorides: In situ NMR measurements and molecular dynamics simulations, Phys. Chem. Chem. Phys. 11 (48) (2009) 11501–11506.
[76] H. Luo, S. Xiao, S. Wang, P. Huai, H. Deng, W. Hu, Molecular dynamics simulation of diffusion and viscosity of liquid lithium fluoride, Comput. Mater. Sci. 111 (2016) 203–208.
[77] Y. Abe, O. Kosugiyama, A. Nagashima, Viscosity of LiF-BeF2 eutectic mixture (XBeF2=0.328) and LiF single salt at elevated temperatures, J. Nucl. Mater. 99 (2–3) (1981) 173–183.
[78] J. Liu, X. Xiao, Molecular dynamics investigation of thermo-physical properties of molten salt with nanoparticles for solar energy application, Energy 282 (2023) 128732.
[79] M. Vetyukov, G. Sipriya, Viscosity of melts of the systems LiF-AlF3 and NaJAlF6-LiJAlF6, Zhur. Prikl. Khim 36 (1963) 1905–1909.
[80] Z. Jiang, A. Palacios, X. Lei, M. Navarro, G. Qiao, E. Mura, G. Xu, Y. Ding, Novel key parameter for eutectic nitrates based nanofluids selection for concentrating solar power (CSP) systems, Appl. Energy 235 (2019) 529–542.